COMMUNICATION

Check for updates

Data-driven modelling for electrolyte optimisation in dye-sensitised solar cells and photochromic solar cells†

Johan Liotier, [ID] * Antonio J. Riquelme, Valid Mwalukuku, Quentin Huaulmé, Yann Kervella, Renaud Demadrille [ID] * and Cyril Aumaître [ID] *

Because they can be made semi-transparent, dye-sensitised solar cells (DSSCs) have great potential for glazing applications. Their photovoltaic performance and light transmission depend not only on the dye used, but also on the electrolyte they contain. A few years ago, we introduced the concept of solar cells with dynamic optical properties based on the use of photochromic photosensitizers. These cells allow variable light transmission according to sunlight conditions, while producing electrical energy. We found that the electrolytes commonly used in DSSCs are not optimal for this class of photosensitisers and need to be tuned. In this work, we have developed and characterised two new photochromic dyes for use in solar cells and we present a study aimed at developing electrolytes specifically adapted to these dyes. Using a methodology based on the design of experiments (DoE) combined with a machine learning (ML) approach, we show that it is possible to quickly find an optimal formulation for iodine-based electrolytes to achieve good transparency of photochromic devices with an AVT ranging from 57% to 23% across the photochromic process, while keeping the photovoltaic conversion efficiency above 2.9%. We show that this approach can be applied to other classes of electrolytes with different redox systems, such as TEMPO/TEMPO+. After optimisation, TEMPO-based electrolytes yielded photochromic semi-transparent solar cells with a PCE of up to 2.16% and an AVT varying between 55% and 13% and opaque photochromic cells with a PCE of 3.46%. Finally, this new TEMPO-based electrolyte was tested with a non-photochromic dye and gave a PCE of up to 7.64%, which is probably the highest performance to date for a dye solar cell using a pure TEMPO/TEMPO+ redox system.

IRIG-SyMMES, Université Grenoble Alpes, CEA, CNRS, Grenoble INP, Grenoble 38000, France. E-mail: renaud.demadrille@cea.fr, cyril.aumaitre@cea.fr, johan.liotier@livmats.uni-freiburg.de

† Electronic supplementary information (ESI) available: Synthesis procedures, characterization techniques, solar cell fabrication, and machine learning data. See DOI: https://doi.org/10.1039/d4mh01375a

New concepts

Electrolytes play a critical role in energy technologies, but their optimisation is challenging due to the complexity of their formulation and the number of chemical compounds involved. Their optimisation typically requires a large number of experiments, as the effects of these compounds on performance are often correlated and difficult to analyse independently. In this study, we use novel photochromic dyes and, for the first time, develop a new data-driven modelling approach for optimising electrolytes in photovoltaic devices. Using machine learning, we designed electrolytes for photochromic semi-transparent dye-sensitized solar cells that successfully balanced two key properties that are typically difficult to reconcile: visible transparency and power conversion efficiency. Notably, our model required a limited number of experiments to train, and its predictions were experimentally validated with excellent agreement. We further demonstrate that this method can be extended to the design of electrolytes with different redox systems. We also highlight that the optimised formulations can achieve state-of-the-art efficiencies in dye solar cells using classical dyes. We believe that this approach will accelerate the development of high performance electrolytes and may be applicable to other areas of materials science.

Introduction

Since the pioneering work of O'Regan and Grätzel in 1991, much work has been done to improve the performance and stability of dye-sensitized solar cells (DSSCs). The advent of perovskite cells in the last decade has slowed their development, but they are still progressing and remain a promising photovoltaic technology that is well suited to specific applications.[1–4] In 2023, DSSCs have consolidated with a record efficiency of 15.2% under an AM 1.5G solar simulator[5] and over 36% under low light illumination.[6] In addition, these devices have demonstrated remarkable stability over emerging photovoltaics[7] and have shown lifetimes of around 10 years in accelerated ageing tests[1,8–10] and 12 years under outdoor operating conditions.[11]

Their production relies on natural abundant raw materials and simple and low environmental impact processes,[9] making them well suited for industrial development. In addition to their

efficiency and manufacturing process, DSSCs have some specific characteristics that make them very attractive for building integrated photovoltaics (BIPV) or agrivoltaics (Agri-PV).[12–16] These properties include the potential to be scaled up to small modules[17–19] or flexible devices[20] and the possibility of making colourful[1] and semi-transparent solar cells and panels.[21]

Compared with other transparent solar photovoltaic technologies, DSSCs are among the technologies that offer the most advantages in terms of performance and ease of manufacture, while also offering an excellent compromise between transparency and efficiency.[22,23]

In this context, in 2020 we reported the first development of fully reversible photochromic dye solar cells, which can adapt their transparency and solar energy conversion according to light conditions.[24] This first example was based on the development of a diphenyl-naphthopyran photochromic dye, **NPI**, which has served as a benchmark for further studies and a source of inspiration to design new molecules with different properties towards more aesthetic mini-modules.[25–29]

In the course of our work, we discovered that the dyes derived from this photochromic unit did not always work properly with standard iodine-based electrolytes, which often contain numerous additives. We therefore developed a very simple iodine-based electrolyte consisting of molecular iodine (I_2) and lithium iodide (LiI) for use with these dyes.[24]

When developing semi-transparent solar cells, it is essential to optimize not only the photovoltaic performance but also the optical properties of these cells. This is particularly true for glazing applications. The photochromic dye is not the only component that can affect the transparency of the device, the electrolyte is very often the element that reduces the transmission of light through the cell. In order to improve the efficiency and the transparency of the device, it is essential to optimize the formulation of the electrolyte. The main active element in the electrolyte solution is the redox couple required for the dye regeneration process. The most commonly used pair is I^-/I_3^-,[1,2,10] using acetonitrile (ACN) as the solvent,[30] while other redox pairs such as Co^{2+}/Co^{3+},[31–33] Cu^+/Cu^{2+},[34–36] or aqueous TEMPO/TEMPO$^+$ have been explored in the literature.[37] Although the performance of Co^{2+}/Co^{3+} and Cu^+/Cu^{2+} with classical dyes is the best, the misalignment of their energy levels with our photochromic dyes, the need to prepare optimized electrodes with adapted pore size and their high absorbency limit their interest for the time being. The electrolyte solution usually contains various additives that are not involved in the regeneration process but used to increase the efficiency of the device,[38–42] generally by shifting the conduction band of the semiconductor, or preventing the interfacial recombination processes.[43] All the developments made with classical dyes need to be revisited and re-examined in the case of photochromic dyes, as they can interact with some additives that may interfere with the opening of the photochromic dye.[27] In addition, the energy levels of some naphthopyran dyes in the coloured state do not always match well with the metal oxide conduction band, leading to injection problems. Therefore, most of the commonly used additives, which are often introduced to shift the energy level

of the conduction band of the TiO_2, are not recommended when using this family of dyes. However, lithium ions can be very helpful in increasing the conductivity of the metal oxide.[44] In our home-made (HM) electrolyte, LiI acts both as one of the redox pairing elements and as the source of these lithium ions. However, the high concentration of this compound is detrimental to the transparency of the electrolyte and therefore to the device. For this reason, other sources of lithium such as bis(trifluoromethanesulfonyl)imide (LiTFSI)[45] can be explored, to reduce the amount of LiI in the electrolyte. The main problem remains that changing an electrolyte component affects both performance and optics, making its optimization doubly complex due to their interdependence. In order to find the best compromise between transparency and efficiency, it is necessary to replace LiI by LiTFSI and to optimize its concentration, taking into account the dual role of LiI, both as a crucial element of the redox pair and as an enhancer of the conductivity of TiO_2. Given the enormous number of potential experiments required to optimize an electrolyte composed of different elements, a way to focus these efforts is needed. In this way, machine learning (ML) approaches have been widely used to optimize various PV technologies[46,47] such as perovskite solar cells (PSCs),[48–50] organic photovoltaics (OPVs)[51–54] or DSSCs.[55–57] They can also be used to search for new chemical structures, but more computational data are needed to identify new efficient molecules.[58–60]

In two seminal papers, Buriak *et al.*[61,62] reported a simple optimization method based on the application of machine learning techniques to the results of design of experiments (DoE). It generates multi-dimensional maps that allow unbiased observation not only of the regions or areas with the "best" performance, but also of new areas that have not yet been explored. The DoE is used to reduce the number of experiments used for optimization while exploring a wide range of target parameters. In order to optimize both parameters (photovoltaic performance/aesthetic characteristics) with the same set of experiments, we have chosen this method.

In this work, we present the synthesis and characterization of two new photochromic dyes for use in dye-sensitised solar cells. We then present a study aimed at developing electrolytes adapted to these dyes, based on experimental designs combined with a machine learning method. Using this strategy, we demonstrate that it is possible to simultaneously optimize the content of I_2, LiI and LiTFSI within the electrolyte with a limited number of experiments and to find an optimal formulation to achieve good device transparency while optimizing the photovoltaic conversion efficiency. Finally, we show that this methodology can be extended to the design and rapid optimisation of other electrolytes using redox pairs for which there is less data available in the literature, such as the TEMPO/TEMPO$^+$ pair. Using this strategy with a classical dye, we achieved the highest efficiency ever reported with TEMPO based electrolyte.

Synthesis and optoelectronic properties of novel photochromic dyes

In this study, we set out to develop two new photochromic dyes and compare their properties and photovoltaic performance

with **NPI**,[24] our previously reported dye used as a reference here. The two dyes **JoLi125** and **QH138** belong to the diphenyl-naphthopyran series; their chemical structures are shown in Fig. 1. **JoLi125** differs from **NPI** by the presence of a triphenylamine moiety used as a donor group instead of the diphenylamine unit. For **QH138**, in addition to replacing the diphenylamine (DPA) group with a triphenylamine (TPA), the core of the photochromic dye was modified with a thiophene instead of a benzene to fuse with the indene group. These modifications are expected to shift the absorption spectrum of the open form isomers and give dyes with different hues.

Both photochromic dyes are obtained by a convergent synthetic strategy. The classical approach for the preparation of the dyes **JoLi125** and **QH138** involves the preparation and use of two essential building blocks: the central indenonaphthalene moiety together with either a phenyl or a thiophene moiety. The synthetic route to the dyes is shown in Fig. 1, together with the chemical structure of **NPI** used as a reference dye. All synthetic procedures and characterizations are fully described in the ESI.† The synthesis of the protected naphthols **N1** and **N2** and their intermediates are presented in the ESI.† The synthesis started with a Suzuki cross-coupling between the brominated indenonaphthalene compound **N1** and *N,N*-diphenyl-4-(4,4,5,5-tetramethyl-1,3,2-dioxaborolan-2-yl)aniline to give compound **1**. This compound was then demethylated with BBr₃ to give compound **2**. A chromenization reaction followed by deprotection of the aldehyde was then carried out between naphthol **2** and a propargyl alcohol to give naphthopyran **3**. This reaction gave a very high yield of 78%, which is remarkable with this reaction on this type of naphthol. Compound **3** was then subjected to Knoevenagel condensation with cyanoacetic acid to give the final dye, **JoLi125**.

As for the previous synthesis, the preparation of **QH138** starts with the reaction of **N2** with *N,N*-diphenyl-4-(4,4,5,5-tetramethyl-1,3,2-dioxaborolan-2-yl)aniline through Suzuki cross-coupling to give compound **7**. Compound **8** is then obtained by demethylation of compound **7** with BBr₃. A chromenization reaction is then carried out with a brominated propargyl alcohol and compound **8** to give compound **9**. Compound **10** was then obtained by Suzuki cross-coupling between compound **9** and 4-(4,4,5,5-tetramethyl-1,3,2-dioxaborolan-2-yl)benzaldehyde. Finally, the dye **QH138** was obtained by a Knoevenagel reaction between compound **10** and cyanoacetic acid.

The optical properties of the dyes were investigated by UV-visible spectroscopy in toluene.

The absorption spectra of the **JoLi125** and **QH138** dyes were compared with those of the **NPI** dye (shown in Fig. 2 and outlined in Table 1).

The dye solutions are measured in both unlit and lit conditions using a polychromatic light source covering a spectrum from long to short wavelengths. This approach has been adopted to mitigate any potential interferences arising from the measurement methodology, such as the possible transformation of the dyes from their closed to open configuration as a result of exposure to UV photons during the measurement process.

In closed form, **NPI** and **JoLi125** show a very similar absorption pattern, but **JoLi125** shows a small hypsochromic shift in the UV spectral region (440 nm *vs.* 450 nm for **NPI**), probably due to the lower conjugation of the TPA moiety compared to the DPA moiety with the rest of the molecule. As expected, the closed form isomer of **QH138** shows a 30 nm bathochromic shift in the onset of the π–π* transition due to the decrease in
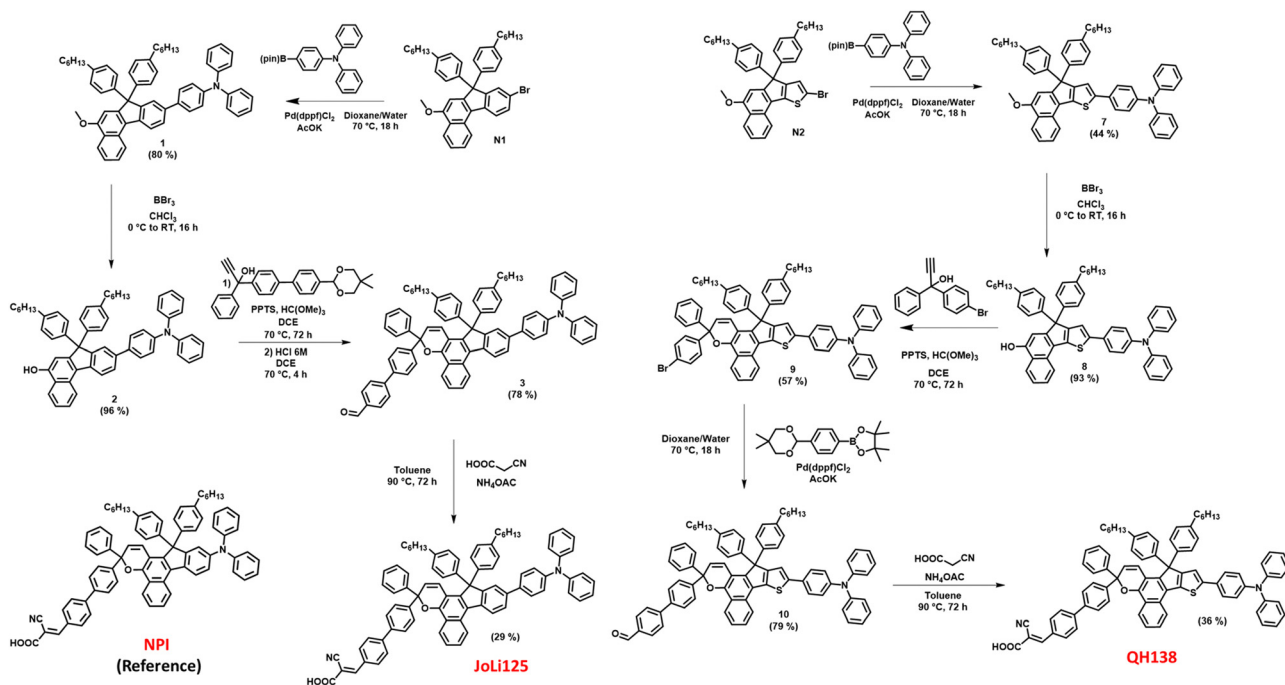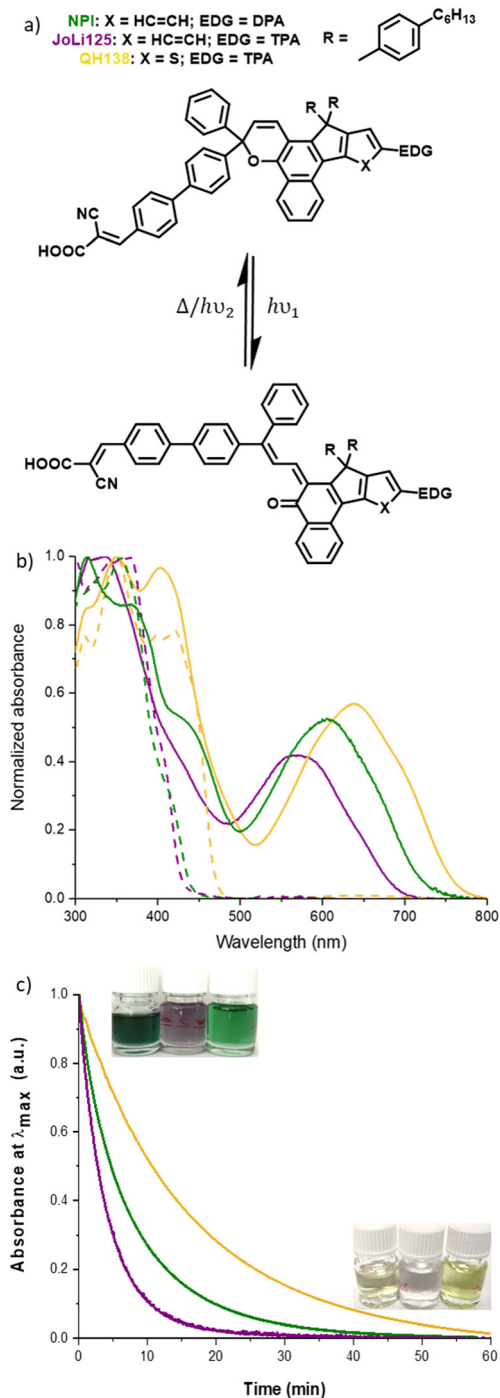

Fig. 1 Synthetic routes and conditions towards **JoLi125** and **QH138** and the chemical structure of **NPI**.

a) **NPI**: X = HC=CH; EDG = DPA
JoLi125: X = HC=CH; EDG = TPA
QH138: X = S; EDG = TPA
R =

Table 1 Table of optical characteristics and photochromic properties of **NPI**, **JoLi125** and **QH138** (toluene, 2×10^{-5} M, 25 °C, irradiance: 200 W, 300–600 nm)

Dyes	λ_{max} CF (nm)	λ_{onset} CF (nm)	λ_{max} OF (nm)	λ_{onset} CF (nm)	ΔE_{opt} OF (eV)	A_{eq}	k (s^{-1})
NPI	318	450	606	728	1.70	0.38	2.1×10^{-3}
JoLi125	370	440	570	700	1.90	0.22	3.8×10^{-3}
QH138	350	470	638	760	1.63	0.67	99×10^{-4}

isomer must absorb photons beyond the absorption limit of the glass substrate and metal oxide film (around 400 nm).[63] By extending the absorption range into the visible, well above 400 nm, the dye is better photo-activated, allowing greater colourability in solution and potentially in devices. However, there is a downside to this feature, as the dye is slightly yellow in color prior to activation.

Under illumination, the photogenerated open form (OF) isomers of the dyes show enhanced delocalisation of the pi-electrons, leading to an extension of the absorption spectrum into the visible region. New transitions appear, in particular a broad shoulder around 450 nm corresponding to a more delocalised π–π* transition. A second broad absorption in the visible region appears, corresponding to an internal charge transfer transition occurring between the donor unit and the acceptor part attributed to the transition between the HOMO and the LUMO of the dyes[29] (see the spatial distribution of electronic density in Fig. S5, ESI†). Interestingly, **QH138** and **JoLi125** exhibit different properties when compared to **NPI**. Under illumination, **JoLi125** exhibits a spectrum with a hypsochromic shift of 36 nm relative to **NPI**, whereas **QH138** exhibits an inverse red shift of 32 nm relative to **NPI**.

Discoloration kinetic constants (*k*-values) were determined in solution by fitting the bleaching curves with a mono-exponential equation (see Fig. 2c). It is evident that **JoLi125** undergoes rapid discoloration. This dye loses approximately 90% of its absorbance within 10 minutes and is completely discolored in approximately 30 minutes. The kinetic constant for **JoLi125** is 3.8×10^{-3} s^{-1}, which represents an 80% increase in the rate of discoloration compared to **NPI**. **QH138**, on the other hand, takes just over an hour to fade completely. About 90% of its color is lost in about 40 minutes. Its kinetic constant of 9.9×10^{-4} s^{-1} indicates a 53% reduction compared to **NPI**. This finding is in agreement with our previous studies where the kinetic constant is found lower with higher donor strength and better planarization of the donor group, leading to a better electronic delocalization through the pi-conjugated system and the stabilization of the open isomers.[29]

In order to study the energy levels of the dyes in both their activated and non-activated states, cyclic voltammetry measurements were carried out under two conditions: (1) in the dark and (2) after irradiation. The measurements were carried out in anhydrous dichloromethane (DCM) with a 0.1 mol L^{-1} solution of TBAPF$_6$ as the supporting electrolyte. An AgNO$_3$ reference electrode was used, while ferrocene was used as an internal reference. The concentration of the dyes was all set to 2×10^{-3} mol L^{-1}.

Fig. 2 (a) UV-vis spectra of **JoLi125** (violet), **QH138** (yellow) and **NPI** (green) in the dark (dashed line) and under irradiation (straight line); (b) bleaching kinetics of **JoLi125** (violet), **QH138** (yellow) and **NPI** (green) at 25 °C after 1 min irradiation (toluene, 2×10^{-5} M, irradiation: 200 W, 300–600 nm). (c) Photochromic interconversion mechanism and picture of the vial containing a solution of **NPI**, **JoLi125** and **QH138** (left to right) before (top) and after (bottom) bleaching.

the torsion angle between the core and donor moiety compared to **Joli125** (see the torsion angle analysis in the ESI†). The position of the absorption edge is important because, for photo-activation in photochromic solar cells, the uncolored

The cyclic voltammograms and the calculated Frontier orbitals are shown in the scheme of Fig. S5 (ESI†). The three compounds were also modelled with DFT calculations (geometry optimization: RevPBE; single point: B3LYP hybrid functional; basis set: TZ2P) in both the open and closed forms. The energy levels of TiO_2 and the redox mediator I^-/I_3^- are also shown.

As expected, the experimental LUMO values are all identical (ca. −3.9 eV) between the three dyes because the acceptor part of the dyes remains unchanged. It remains at a good level for injecting electrons in the TiO_2 conduction band (−4.1 eV), but limits the use of electrolyte additives such as tert-butylpyridine, which can increase the V_{OC} of the device.[64,65] Conversely, the HOMO levels show an evolution as a function of dye structure, but are all still compatible with the iodine-based redox shuttle (−4.9 eV). Compared to the HOMO energy level of **NPI** (−5.2 eV), the HOMO energy level of **JoLi125** is stabilised (−5.4 eV), confirming a lower donor power of the TPA moiety linked to the indeno-naphthopyran moiety. By replacing the phenyl with a thiophene in the core of **QH138**, we observed a slight increase in the HOMO level (−5.1 eV), confirming the better donor effect of the thiophene and a better conjugation with the donating group due to a more planar structure (see the DFT results in Fig. S3 and S4, ESI†). These observations are in full agreement with the spectra obtained by UV-visible spectroscopy. The electronic density of the three compounds has been modelled with DFT calculations in both open and closed form. The calculated Frontier orbital energy is slightly different from the measured one, but follows the same trend. The HOMO–LUMO separation in the case of **JoLi125** and **QH138** is similar to that of **NPI** (see Fig. S5, ESI†).

Photovoltaic and optical performances

In order to evaluate the photovoltaic performance and the optical properties of the newly developed photochromic dyes, transparent DSSCs (13 μm-thick, transparent mesoporous layer only) were fabricated. Further experimental details on the fabrication and characterization of the solar cells can be found in the ESI.† All the dyes were tested under the same device configuration and with the same ratio of chenodeoxycholic acid (CDCA). Their performance was compared to that of **NPI**, which served as the reference dye. The current–voltage characteristics are recorded at different time intervals of light exposure (AM 1.5G, 1000 W m^{-2}) until the photostationary state (PSS) is reached, corresponding to the stabilisation of the photochromic equilibrium. The efficiencies obtained at a CDCA/dye ratio of 1:10 are shown in Table 2 (and the corresponding J–V curves are shown in Fig. S11, ESI†). To evaluate the optical properties of the dyes, we measured the average visible transmission (AVT) of the complete solar cells before irradiation. The AVT provides insight into light transmission across the visible spectrum and for their applications as smart windows for building integrated photovoltaics. Transmittance curves were recorded for these cells and are presented in the ESI.† Although PCE and AVT are often inversely related, it is becoming increasingly complex to analyse this relationship and clearly identify the dye that offers the best compromise, particularly in the case of photochromic dyes because of their ability to adapt their absorption to changing light conditions. For this reason, the relationship between AVT and PCE changes before and after irradiation and also as a function of light intensity. In order to evaluate our dyes, we propose an evaluation of the efficiency of light use adapted from Traverse et al.[66] with this equation:

$$C^* = \frac{AVT_{closed}}{AVT_{open}} \quad LUE_p = C^* \times PCE$$

where C^* represents the colourability of the molecule in the complete device, as it analyses the difference between the uncolored and the colored state. This metric (shown in Table 2) is used to estimate the light-utilization efficiency (LUE_p) of a photochromic device.

To study the performances of these dyes in semi-transparent device configuration, we tested those dyes with our home-made (HM) electrolyte (90 mmol L^{-1} of I_2 and 0.5 mol L^{-1} of LiI in acetonitrile (ACN)). It can be seen that the cells obtained with **JoLi125** are less efficient than those obtained with **NPI**. In fact, with **JoLi125** we obtained a PCE of 2.04%, whereas with **NPI** we obtained a PCE of 3.57% with similar V_{OC}. The decrease in performance is due to a twofold decrease in current density compared to **NPI** (5.96 mA cm^{-2} compared to 11.85 mA cm^{-2}), which could be explained by a narrower absorption in the open form and lower colourability. In the case of **QH138**, the PCE is better (2.60%) than **JoLi125** but still lower than **NPI**. The optical characteristics of these cells are shown in Table 2. In all the devices, the absorption of iodine and the titanium oxide layer is an important factor explaining the moderate transparency. As expected, **QH138** before activation shows a slightly lower AVT due to the absorption shoulder between 400–500 nm. After irradiation, we see that the transparency of the cells decreases by 11% for **QH138**, while for **NPI** and **JoLi125** it decreases by 20% and 29% respectively.

These observations are consistent with the photochromic and optical properties of these dyes recorded in solution. Switching from a strong electron donating group (DPA) in **NPI** to a weaker one (TPA) in **JoLi125** tends to destabilize the open form, leading to a faster thermal closure mechanism. Conversely, replacing the benzene ring in the indenonaphthalene core with a thiophene in **QH138** has the opposite effect. The flattening of the dihedral angle between the donor group

Table 2 Table of electrical characteristics of semitransparent solar cells made with **NPI**, **JoLi125** and **QH138** (Dye/CDCA ratio: 1/10)

Dyes	J_{SC} (mA cm^{-2})	V_{OC} (mV)	FF (%)	PCE (%)	AVT$_{closed}$ (%)	AVT$_{open}$ (%)	C^*	LUE$_p$
NPI	11.85 (11.84 ± 0.01)	505 (499 ± 9)	60 (60.0 ± 0)	3.57 (3.51 ± 0.09)	51	31	1.6	5.7
JoLi125	5.96 (5.91 ± 0.07)	509 (500 ± 12)	67.0 (68.3 ± 1.8)	2.04 (2.02 ± 0.03)	60	31	1.9	3.9
QH138	8.98 (8.77 ± 0.30)	487 (497 ± 14)	59 (58.0 ± 2)	2.60 (2.53 ± 0.11)	50	29	1.72	4.4

and the indeno-thiophene moiety increases the conjugation path to the acceptor moiety, improving electronic density delocalization and stabilizing the open form.[67]

This behaviour results in a bathochromic and hyperchromic shift of the ICT transition and slows the thermal return to the closed form. In summary, **Joli125** and **QH138** show lower performance than our reference **NPI** without any optimization, but **QH138** exhibits very promising optical properties that could lead to better performance once device manufacturing is optimized. Indeed, our reference dye **NPI** reaches a LUE_p value of 5.7 while **QH138** and **JoLi125** shows lower LUE_p values of 4.4 and 3.9, respectively. At this point, we decided to focus on **QH138** and optimize the electrolyte to maximize its efficiency while keeping the AVT of the device as high as possible. However, the composition of the electrolyte is a complex formulation requiring the optimization of many parameters. In addition to the redox couple used, additives or salts can be used to improve performance or stability.[42,68,69] Optimization is generally aimed at either photovoltaic performance or transparency, but never both at the same time.[70] The large number of parameters to be considered leads to a large number of experiments and requires the development of a clear methodology.

Data driven assisted modelling of the iodine based electrolyte

In this work, we chose to adapt the data-driven assisted modelling method proposed by Buriak *et al.*[61] to optimize the iodine-based electrolyte specifically for **QH138**. This approach is based on a supervised machine learning program using a classification algorithm. With this method, we can draw several efficiency maps depending on the target parameter values. In order to provide a robust set of training data, we rationalized our approach with a design of experiment (DoE) approach and avoided experimenting with one factor/one variable at a time. This was done by carefully choosing the different parameters based on our knowledge. We also carefully designed an experimental plan with experiments covering all dimensions of the variables, even the worst possible experiments that will provide useful information for the algorithm.

Initially, our home-made electrolyte consists of molecular iodine at a concentration of 90 mmol L^{-1} and lithium iodide at a concentration of 0.5 mol L^{-1} in acetonitrile. The molecular iodine is used as a redox couple, while the lithium iodide provides a source of iodide ions in the electrolyte and also interacts with the titanium oxide layer, which slightly tunes the level of its conduction band to obtain better injection and better J_{sc}.[27] From these two sources, the yellowish molecular iodine in solution is the main problem for transparency. An alternative is the replacement of lithium iodide with lithium bis(trifluoromethanesulphonyl)imide (LiTFSI). This salt could help in reducing the amount of lithium iodide, which would decrease the amount of iodide ions without reducing the amount of lithium ions.

For the first round of optimization, three values were chosen around the initial values for each parameter. The molecular iodine concentration was set at 60, 90 and 120 mmol L^{-1}; the lithium iodide concentration was set at 0.1, 0.3 and 0.5 mol L^{-1}

and the LiTFSI concentration was set at 0, 0.15 and 0.3 mol L^{-1}. We kept acetonitrile as the electrolyte solvent. A full factorial would require 27 experiments to investigate all the parameters. Here we chose a semi-factorial design with 13 experiments (full table available in the ESI†). Each experiment was repeated twice for reproducibility, and the power conversion efficiency (PCE) and average visible transmittance (AVT) were recorded using the same procedure and reported in the ESI† (see Table S1).

As a first observation, the PCE of the devices ranged from 0% to 2.72%. Most of the conditions tested gave PCEs around 2%. In fact, only four conditions gave low results: 1–3 (0%), 1–4 (0%), 1–10 (0.7%) and 1–12 (0.52%). In terms of AVT, they are all greater than 51%, except in the case of experiments 1–3 and 1–4, where the AVT is 39.1% and 31.5% respectively. These two points correspond to a high concentration of molecular iodine (90 mmol L^{-1} for experiment 1–3 and 120 mmol L^{-1} for experiment 1–4) with a low concentration of lithium iodide (0.1 mol L^{-1} in both experiments). It should be noted that this combination led to the activation of the molecule without irradiation. In fact, when the electrolyte was added, the corresponding cells showed the characteristic green color of the molecule opening under irradiation, which explains the low AVT obtained. This coloring also had a negative effect on the PCE of the cell. This behaviour could be explained by the ionochromic nature of certain photochromic dyes.[71,72] In fact, it is possible that the molecule tends to form stable complexes with iodine ions in open form, leaving a greenish colouration and increasing recombination due to the high concentration of iodine. An analysis of variance (ANOVA) was performed to determine the relative importance of each parameter on the output parameters (PCE, AVT) and the results are presented in Fig. 3.

In the case of PCE, the graph shows that within the range of concentrations used, the lithium iodide concentration is the major contributor to cell efficiency. In fact, this concentration accounts for 98% of the expected variance. The LiTFSI concentration also appears to have a small effect on efficiency, with a fraction of variance of around 1.9%.

With a fraction of variance of less than 0.1%, the molecular iodine concentration had no influence on the cell PCE, showing that the electrolyte is saturated in this concentration range. In the case of AVT, the importance of the lithium iodide concentration is again evident. However, the proportion of variance for this lithium iodide concentration is lower than for PCE with a proportion of 57%. This time the molecular iodine concentration accounts for a larger proportion of the variance fraction with 32% of the variance. The fact that these two concentrations account for the majority of the variance in the case of the AVT analysis is logical, as these are two parameters that form the colored redox couple. Finally, the LiTFSI concentration accounted for only 11% of the variance. These results were fed as training data into our updated homegrown Python program to generate our output data, which can then be plotted (available in the ESI†). The results were plotted with PCE and AVT as output and presented in Fig. 4.

Regarding the PCE, it can be seen that a low lithium iodide concentration (less than 0.15 mmol L^{-1}) induces a very low
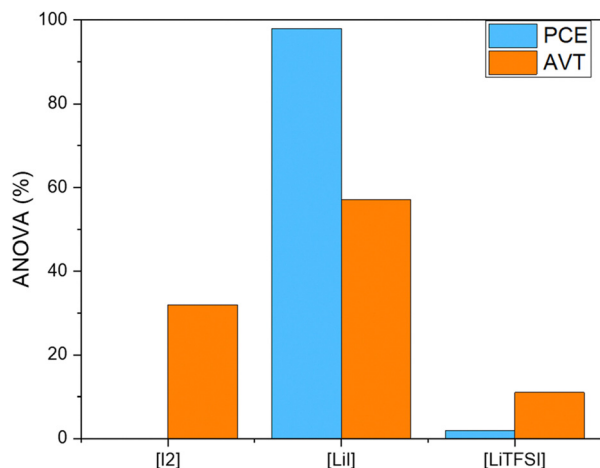
Fig. 3 Analysis of variance and factor evaluation of the first round of optimization of the iodine-based electrolyte for **QH138**-dyed solar cells.

efficiency, regardless of the molecular iodine concentration. We can see that in each panel the efficiency is highest in the lower right corner where the LiI concentration is between 0.3 and 0.5 mol L^{-1} and the LiTFSI concentration is between 0 and 0.15 mol L^{-1}. The maximum efficiency that seems to be achievable is at a concentration of 60 mmol L^{-1}. Indeed, we observe a zone where the efficiencies are greater than 2.7% with a LiI concentration between 0.4 and 0.5 mol L^{-1} and a LiTFSI concentration between 0 and 0.1 mol L^{-1}. In the case of AVT, it should be noted that areas of low AVT values are found when the LiI concentration is low compared to the I_2 concentration. For iodine concentrations of 90 and 120 mmol L^{-1}, it can be seen that the AVT cannot exceed 52%, whereas for a concentration of 60 mmol L^{-1} there are areas where AVT can be higher than 54%. Better transparency can therefore be obtained with an iodine concentration of 60 mmol L^{-1}.

We can see from the two analyses that the best values for each result are obtained with an I_2 concentration of 60 mmol L^{-1}. A zone seems interesting to explore for obtaining an even higher PCE and a satisfactory AVT (>54%). In order to refine our optimization, we decided to run 4 more experiments in the zone of interest. These new experiments 2–1 to 2–4 are shown in the ESI† together with their results. The same process as before was repeated with the new set of experiments including the new data points. The ANOVA is similar to the one obtained in the previous paragraph and the program was trained again. With this second set of data we improve the accuracy of our model and identify the best recipe for our electrolyte with the following composition: [I2] = 60 mmol L^{-1}, [LiI] = 0.45 mol L^{-1} and [LiTFSI] = 0.02 mol L^{-1}. This composition is assumed to give an efficiency of 2.74%. On the AVT surface, this composition gives a transparency of around 54%, which is close to the maximum achievable of 54.4%. To confirm our predictions, solar cells were fabricated with the optimal electrolyte (hereafter El_{opt}) and compared with our HM electrolyte, and the results are summarized in Table 3. Surprisingly, the El_{opt}-based device reached a PCE of 2.94% that is higher than the value anticipated by the program (2.74%).

This performance is 20% higher than that obtained with the HM electrolyte, with 16% less iodine. This increase is due to a rise in J_{sc} from 10.57 mA cm^{-2} with HM to 12.08 mA cm^{-2} with El_{opt}. In synergy with the photovoltaic performance, optical properties have also been improved before and after photo-activation. The colourability of the photochromic cells has been improved by almost 1.5 times and the overall light utilization efficiency by almost 2 times. It seems that even at 60 mM iodine, we are already at a concentration that saturates absorption at certain wavelengths and that this concentration would have to be drastically reduced to see any significant effect on AVT, although when the cell is irradiated, a slight difference is observed as we obtain an AVT of 29% with HM and 23% with El_{opt}. These results argue in favor of a radical change in the electrolyte composition to optimize both the optical and the photovoltaic performance, so we decided to investigate a new type of electrolyte based on organic redox systems that has been rarely investigated, and to develop a specific formulation for photochromic dyes using the same DoE-ML approach.

Development and optimization of a TEMPO-based electrolyte

Having successfully used the DoE-ML approach to optimize an iodine-based electrolyte from the well-known LiI/I_2 electrolyte, we wanted to change the redox mediator and validate the usefulness of this approach by optimizing from scratch a new electrolyte for photochromic DSSCs based on the TEMPO redox couple. Various redox shuttles are commonly used as the main electrolyte element in DSSCs. However, the two most popular options, apart from iodine-based systems, have characteristics that discourage their use in this work. Copper-based electrolytes produce very high efficiencies, but their high colourability would work against the optical properties of semi-transparent devices, and their reactivity with Pt-coated counter-electrodes can cause stability problems.[19,34] On the other hand, cobalt-based electrolytes are very transparent and stable,[32] but the large size of the cobalt complexes implies that the porosity of the electrode should also be optimised,[73] adding complexity to the DoE approach beyond the scope of this work. We chose to use the TEMPO/TEMPO$^+$ because it has been used for electrolyte design in DSSCs and has the advantage of being soluble in water[14] although it can also be used in acetonitrile.[24] Surprisingly, only a few examples of TEMPO-based electrolyte DSSCs have been reported in the literature and these articles mainly focus on performance.[37,74,75] A literature review suggests that the electrolyte composition has never been optimized and that there is relatively little information on the composition of electrolytes using TEMPO/TEMPO$^+$ as a redox mediator. In order to cover a large data set, we chose to optimize four different parameters at four levels. However, this time the full factorial design required 4^4 experiments (in other words, the manufacture of 256 different solar cells, which should be at least doubled for reliability). In this case, in order to reduce the number of experiments to a manageable number, it was decided to use an orthogonal Latin square design to drastically reduce the number of experiments. With this type of design, only 16 experiments were needed for the first optimization.
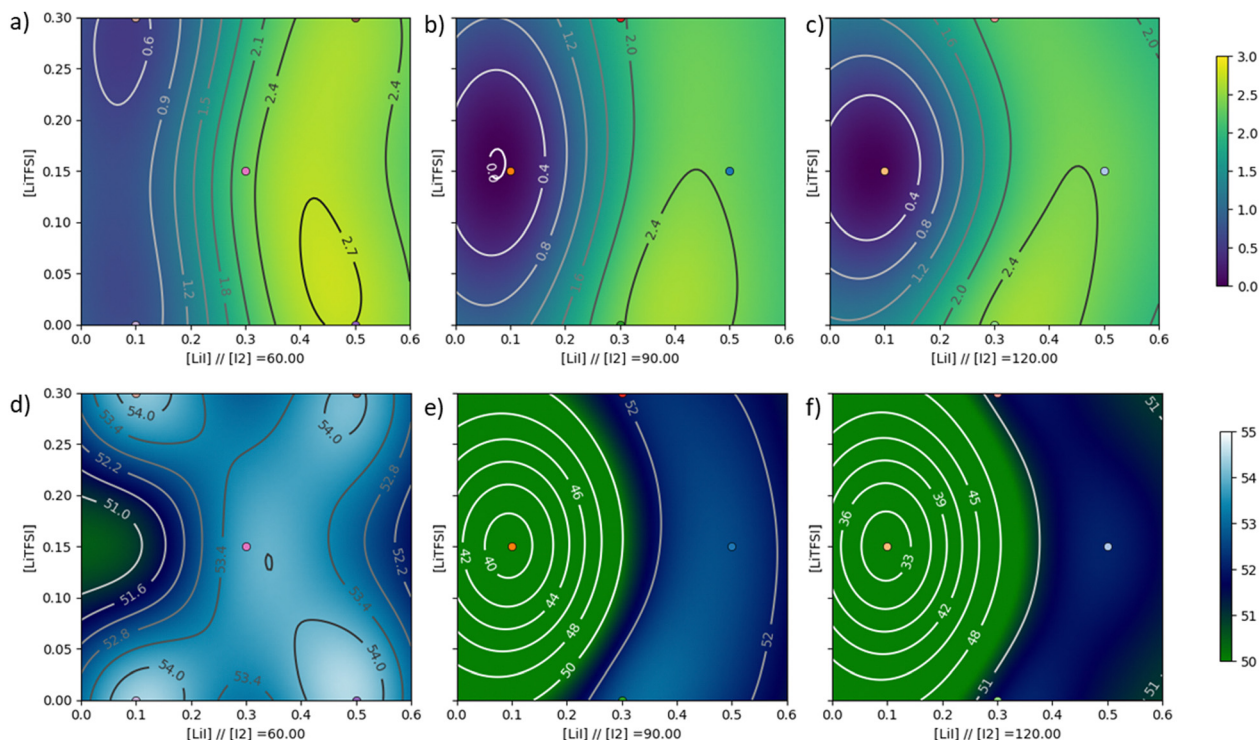
Fig. 4 Support vector machine/radial basis function models were used to fit the experimental data for the two optimization parameters in the initial round: lithium iodine concentration on the x-axis, LiTFSI concentration on the y-axis, and iodine concentration plotted across columns labeled as (a) and (d) 60 mM, (b) and (e) 90 mM, and (c) and (f) 120 mM. The rows correspond to two different output values: (a)–(c) power conversion efficiency, and (d)–(f) average visible transmission. These parameters were measured from devices produced through the design of experiments (DoE) and are represented as dots on the map.

Table 3 Electrical characteristics of solar cells made with **QH138** and the two different electrolytes (HM and El$_{opt}$) (Dye/CDCA ratio: 1/10)

Electrolyte	J_{SC} (mA cm^{-2})	V_{OC} (mV)	FF (%)	PCE (%)	AVT$_{closed}$ (%)	AVT$_{open}$ (%)	$C^\star$	LUE$_p$
HM	8.98 (8.77 ± 0.30)	487 (497 ± 14)	59 (58.0 ± 2)	2.60 (2.53 ± 0.11)	50	29	1.72	4.35
El$_{opt}$	12.08 (12.15 ± 0.09)	455 (453 ± 3)	53.4 (52.7 ± 1.0)	2.94 (2.90 ± 0.06)	57	23	2.48	7.19

Of all the parameters, we chose to formulate this electrolyte in acetonitrile so that it could be compared with our previous electrolyte in terms of performance and transparency. The first parameter to be optimized is the concentration of the two species of TEMPO/TEMPO$^+$ redox mediator. Grätzel *et al.* first demonstrated the use of this mediator by oxidizing 10 mol% of TEMPO with NOBF$_4$[76] and a few years later Boschloo *et al.*[74] demonstrated a PCE of 5.4% with **LEG4**, a classical organic dye. For organic dyes, these studies showed that the TEMPO concentration affects the electron lifetime and drastically shifts the V_{OC}. To the best of our knowledge, a TEMPO-based electrolyte has never been used for photochromic dyes and a complete optimization should be undertaken with this new family of photosensitizers. To continue, we have already mentioned the importance of a lithium-ion source to improve performance.[22] To adjust this concentration, two lithium sources were chosen: lithium iodide and LiTFSI, which were already used in the iodine electrolyte. We manufactured the solar cells using the compositions of the electrolytes shown in Table S3 (ESI†). It

should be noted that under irradiation we found that the performance of the photochromic dyes rises rapidly and then declines to stabilize at PSS. This phenomenon is not linked to the degradation of the electrolyte since TEMPO/TEMPO$^+$ was found to be stable under these conditions during the time-frame of the experiment (see the complementary experiment in the ESI†). The evidence of colouration upon opening of the photochromic dye observed in the AVT, in contrast to the IPCE spectra (see the ESI†), suggests the formation of coloured photochromic complexes with a limited electronic injection under prolonged irradiation.

It also should be noted that the initial PCE measurement can be recovered after the full ring closure of the photochromic dye. Consequently, the PCE results described below and used to optimize the electrolyte are those obtained after 15 seconds of irradiation. This choice was made in order to carry out the analysis at higher values in order to obtain a better resolution.

For this study, the PCE and the AVT before and after irradiation were recorded and the experiments were realized

on two devices for each composition for reproducibility. With these measurements, we were able to calculate our LUE_p and to inject all of these data into our program. It allows us to make a clear visualization of our three important parameters (PCE, AVT and LUE_p) *via* mapping of these targets. All the measured results are summarized in Table S3 (ESI†). Analysis of variance (Fig. 5) shows similar trends to the iodide-based electrolyte, with LiI emerging as the most dominant parameter for PCE and LUE_p, while LiTFSI exerts the strongest influence on AVT results.

The components of the TEMPO redox couple appear to have a lesser effect on PCE but a marked effect on AVT and LUE_p. These training data were then used to plot the full maps calculated using our algorithm in Fig. S20–S22 (ESI†) and to focus on the most interesting area in the figure. Focusing on the PCE plot, we can see that a higher concentration of LiTFSI can give a better performance. In fact, on the panels corresponding to LiTFSI concentrations of 0.2 and 0.3 mol L^{-1}, the "islands" giving the best performance correspond to PCEs of 1.5% and 1.8% respectively. It is interesting to note that several different electrolyte compositions can give the same PCE value. This observation highlights the usefulness of this optimization method, which allows several parameters to be optimized simultaneously, as it is easy to overlook one of these islands if the parameters are optimized linearly. In order to refine our model on the local maxima, we decided to add 7 more experiments based on the first optimization (see Table S4, ESI†) to enhance our training data set. The full maps are drawn for the three output parameters (PCE, AVT and LUE_p), with 16 maps corresponding to the 4 levels of the 4 studied parameters. The full figures in high resolution are presented in the ESI† (Fig. S25–S27) and the area of higher interest is shown in Fig. 6.

In terms of PCE, we can observe 3 maximum ranges above 1.5% in the whole parameter space. Among them, one point localised in Fig. 6 can reach 2.1% under these conditions: [LiTFSI] = 0.30 mol L^{-1}, [TEMPOBF$_4$] = 0.03 mol L^{-1}, [TEMPO] = 0.15 mol L^{-1} and [LiI] = 1.1 mol L^{-1}. This point would also

Fig. 6 Support vector machine/radial basis function models were used to fit the experimental data for the three optimization parameters in the initial round: lithium iodine concentration on the *x*-axis, TEMPO concentration on the *y*-axis. The content of TEMPO+ and LiTFSI are fixed at 0.03 mol L^{-1} and 0.3 mol L^{-1} respectively. The rows correspond to three different output values: (a) power conversion efficiency, (b) average visible transmission, and (c) photochromic light utilization efficiency. These parameters were measured from devices produced through the design of experiments (DoE) and are represented as dots on the map. (d) Resumed results obtained with the optimized electrolyte ([LiTFSI] = 0.30 mol L^{-1}, [TEMPOBF4] = 0.03 mol L^{-1}, [TEMPO] = 0.15 mol L^{-1}, [LiI] = 1.1 mol L^{-1}).

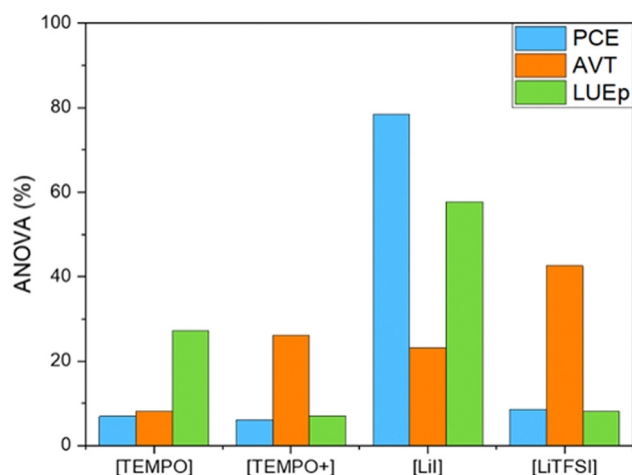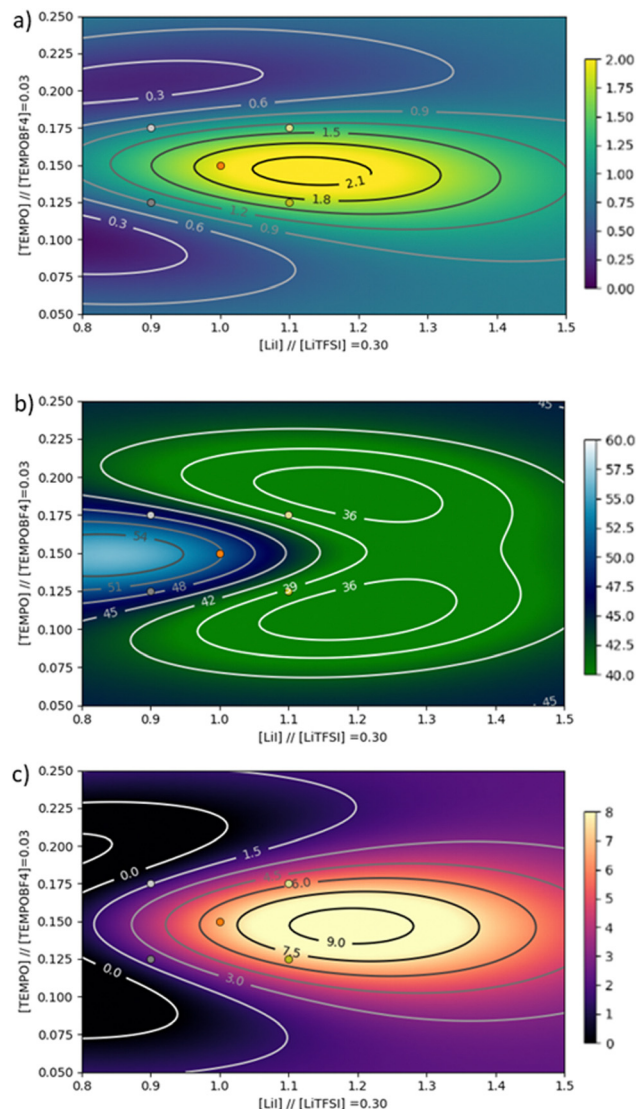

Fig. 5 Analysis of variance and factor evaluation of the first round of optimization of the TEMPO-based electrolyte for **QH138**-dyed solar cells.

correspond to a maximum LUE_p above 9 and an AVT$_{closed}$ around 55%. The final round of optimization predicted a theoretical maximum PCE in excess of 2.1%. When these conditions were tested, an average PCE of 2.03% was found, with a champion efficiency of 2.16% and a LUE_p of 9.12, confirming the model predictions (see Table S5, ESI†).

Although these performances are still modest, they are the first to be obtained using a TEMPO-based electrolyte and a photochromic dye. It should also be borne in mind that the "record" achieved in the literature with TEMPO/TEMPO$^+$ used

Table 4 Photovoltaic parameters of opaque cells with photochromic and classical dyes with TEMPO-based electrolyte compared to the current state of the art

Dye	J_{SC} (mA cm^{-2})	V_{OC} (mV)	FF (%)	PCE (%)	Ref.
QH138	6.87 (6.62 ± 0.35)	651 (650 ± 2)	77.30 (72.85 ± 6.29)	3.46 (3.15 ± 0.44)	This work
YKP88	17.35 (17.62 ± 0.37)	643 (640 ± 5)	68.51 (67.85 ± 0.93)	7.64 (7.64 ± 0.007)	This work
LEG4-T	7.74	965	73	5.43	74

as a single redox mediator and a conventional dye is 5.4% and that this result was obtained on opaque cells, *i.e.* cells with a scattering layer.[74] To demonstrate the relevance of our approach, and to be able to compare our results with the literature, we completed this study by making opaque cells with **QH138** using the composition of our optimized electrolytes. We also chose to use a classic dye from our laboratory, **YKP88**. Combining this electrolyte with the photochromic dye **QH138** produced an efficiency of 3.46% on opaque devices, only 0.70% away from the record efficiency of photochromic dye-sensitized solar cells, even using iodine-based electrolyte.[28] As can be found in ESI,† the IPCE spectra produced integrated photocurrents of 15 mA cm^{-2} and 6.25 mA cm^{-2} for **YKP88** and **QH138**, respectively, which is within the usual range of variation compared to the J_{sc} reported in Table 4.[77] Moreover, attending to the ideality factor, extracted from the dependence of V_{oc} with the J_{sc} at different light intensities, it can be observed that in all cases the values approach unity, evidencing the effect of the lithium species on the TiO$_2$ conduction band.[78]

Regarding the results obtained with **YKP88**, which is a conventional non-photochromic dye, it should be noted that the efficiency obtained exceeds by 40% the highest efficiency reported with TEMPO/TEMPO$^+$ as a redox pair, to the best of our knowledge.[74] It should also be noted that the **QH138** based photochromic devices, using the optimized TEMPO/TEMPO$^+$ electrolyte reached an efficiency of 3.46%, which is not far from the record efficiency reported on photochromic dyes established at 4.16%.[28]

Conclusion

In this work, we have synthesised and fully characterized two new photochromic dyes for use as photosensitizers in dye solar cells. One of these dyes, **QH138**, exhibits a shifted absorption towards longer wavelengths up to 800 nm and a hyperchromic effect in the visible region, compared to **NPI** our reference photochromic dye.

This makes it a good candidate for achieving high performance in semi-transparent photochromic DSSCs.

The home-made iodine-based electrolyte previously developed for **NPI**, which resulted in a PCE of around 3.6%, did not appear to be optimal for **QH138**, and resulted in a PCE of around 2.6%. To speed up the development of a more efficient electrolyte for this new photochromic dye, we set up a method based on design or experimentation and machine learning that allows the photovoltaic performance and optical properties of solar cells to be optimised simultaneously. Using this method, we were able to tune the formulation of the iodine-based

electrolyte and increase the performance of the photochromic devices by 20%, while keeping the AVT before activation of the cell, and the LUE$_p$ high. This new method allowed us to do this with a relatively small number of trials.

To show that this approach can be applied to other classes of electrolytes with different redox systems, we have designed from scratch an efficient TEMPO-based electrolyte for photochromic solar cells. This electrolyte, after optimisation with **QH138**, gave a PCE of 2.16% and a high LUE$_p$ of 9 in semi-transparent cells and a PCE of 3.46% when used in opaque cells. Finally, this new TEMPO-based electrolyte was tested with a non-photochromic dye **YKP88** and gave a PCE of up to 7.64%, which is probably the highest performance to date for a dye solar cell using a pure TEMPO/TEMPO$^+$ redox system.

Author contributions

J. L., Q. H. and Y. K. synthesized and characterized the dyes. J. L. performed the DFT calculations. J. L., A. J. R. and V. M. fabricated the devices and characterized them. J. L. and C. A. coded the python program. R. D., C. A. and J. L. supervised the work, designed the experiments, analysed the data, wrote and edited the manuscript. R. D. acquired the funding. All the authors contributed to the work and gave approval to the manuscript before submission.

Data availability

The ESI† contains all experimental details, including the synthetic methods, and characterization of all chemical products reported in this study. ESI† also includes cyclic voltammetry and DFT calculation data, solar cells preparation and characterisation protocols, *J-V* and transmittance curves for cells prepared with NPI, JoLi125, QH138, and iodine-based electrolyte and TEMPO-based electrolyte optimisation data. The stability data for devices using the TEMPO electrolyte. Raw data for the characterisation of materials and solar cells are available without restriction from the corresponding authors upon request. The python program and the data developed and used in this work are available in GitHub (**https://github.com/Johan Liotier/MachineLearning_Optimisation.git**).

Conflicts of interest

The authors declare no conflicts of interest.

Acknowledgements

References

1 A. Hagfeldt, G. Boschloo, L. Sun, L. Kloo and H. Pettersson, *Chem. Rev.*, 2010, **110**, 6595–6663.

2 A. B. Muñoz-García, I. Benesperi, G. Boschloo, J. J. Concepcion, J. H. Delcamp, E. A. Gibson, G. J. Meyer, M. Pavone, H. Pettersson, A. Hagfeldt and M. Freitag, *Chem. Soc. Rev.*, 2021, **50**, 12450–12550.

3 S. Yun, Y. Qin, A. R. Uhl, N. Vlachopoulos, M. Yin, D. Li, X. Han and A. Hagfeldt, *Energy Environ. Sci.*, 2018, **11**, 476–526.

4 J. Barichello, P. Mariani, L. Vesce, D. Spadaro, I. Citro, F. Matteocci, A. Bartolotta, A. D. Carlo and G. Calogero, *J. Mater. Chem. C*, 2024, **12**, 2317–2349.

5 Y. Ren, D. Zhang, J. Suo, Y. Cao, F. T. Eickemeyer, N. Vlachopoulos, S. M. Zakeeruddin, A. Hagfeldt and M. Grätzel, *Nature*, 2023, **613**, 60–65.

6 H. Michaels, M. Rinderle, I. Benesperi, R. Freitag, A. Gagliardi and M. Freitag, *Chem. Sci.*, 2023, **14**, 5350–5360.

7 N. Kato, K. Higuchi, H. Tanaka, J. Nakajima, T. Sano and T. Toyoda, *Solar Energy Mater. and Sol Cells*, 2011, **95**, 301–305.

8 D. Joly, L. Pellejà, S. Narbey, F. Oswald, J. Chiron, J. N. Clifford, E. Palomares and R. Demadrille, *Sci. Rep.*, 2014, **4**, 4033.

9 R. Harikisun and H. Desilvestro, *Sol. Energy*, 2011, **85**, 1179–1188.

10 F. Sauvage, *Adv. Chem.*, 2014, **2014**, 939525.

11 N. Kato, H. Tanaka, Y. Takeda, K. Higuchi and J. Nakajima, *ACS Sustainable Chem. Eng.*, 2023, **11**, 5014–5022.

12 D. A. Chalkias, C. Charalampopoulos, A. K. Andreopoulou, A. Karavioti and E. Stathatos, *J. Power Sources*, 2021, **496**, 229842.

13 A. Henemann, *Renew. Energy Focus*, 2008, **9**, 14–19.

14 S. Yoon, S. Tak, J. Kim, Y. Jun, K. Kang and J. Park, *Build. Environ.*, 2011, **46**, 1899–1904.

15 M. Pagliaro, R. Ciriminna and G. Palmisano, *Prog. Photovoltaics Res. Appl.*, 2010, **18**, 61–72.

16 H. M. Lee and J. H. Yoon, *Appl. Energy*, 2018, **225**, 1013–1021.

17 A. Fakharuddin, R. Jose, T. M. Brown, F. Fabregat-Santiago and J. Bisquert, *Energy Environ. Sci.*, 2014, **7**, 3952–3981.

18 R. Escalante, D. Pourjafari, D. Reyes-Coronado and G. Oskam, *J. Renewable Sustainable Energy*, 2016, **8**, 023704.

19 C. A. Gonzalez-Flores, D. Pourjafari, R. Escalante, E. J. Canto-Aguilar, A. V. Poot, J. M. Andres Castán, Y. Kervella, R. Demadrille, A. J. Riquelme, J. A. Anta and G. Oskam, *ACS Appl. Energy Mater.*, 2022, **5**, 14092–14106.

20 F. Bittner, T. Oekermann and M. Wark, *Materials*, 2018, **11**, 232.

21 L. Vesce, P. Mariani, M. Calamante, A. Dessì, A. Mordini, L. Zani and A. D. Carlo, *Sol. RRL*, 2022, **6**, 2200403.

22 A. A. F. Husain, W. Z. W. Hasan, S. Shafie, M. N. Hamidon and S. S. Pandey, *Renewable Sustainable Energy Rev.*, 2018, **94**, 779–791.

23 E. Pulli, E. Rozzi and F. Bella, *Energy Convers. Manage.*, 2020, **219**, 112982.

24 Q. Huaulmé, V. M. Mwalukuku, D. Joly, J. Liotier, Y. Kervella, P. Maldivi, S. Narbey, F. Oswald, A. J. Riquelme, J. A. Anta and R. Demadrille, *Nat. Energy*, 2020, **5**, 468–477.

25 A. J. Riquelme, V. M. Mwalukuku, P. Sánchez-Fernández, J. Liotier, R. Escalante, G. Oskam, R. Demadrille and J. A. Anta, *ACS Appl. Energy Mater.*, 2021, **4**, 8941–8952.

26 J. Liotier, V. M. Mwalukuku, S. Fauvel, A. J. Riquelme, J. A. Anta, P. Maldivi and R. Demadrille, *Sol. RRL*, 2022, **6**, 2100929.

27 J.-M. A. Castán, V. M. Mwalukuku, A. J. Riquelme, J. Liotier, Q. Huaulmé, J. A. Anta, P. Maldivi and R. Demadrille, *Mater. Chem. Front.*, 2022, **6**, 2994–3005.

28 V. M. Mwalukuku, J. Liotier, A. J. Riquelme, Y. Kervella, Q. Huaulmé, A. Haurez, S. Narbey, J. A. Anta and R. Demadrille, *Adv. Energy Mater.*, 2023, **13**, 2203651.

29 S. Fauvel, A. J. Riquelme, J.-M. A. Castán, V. M. Mwalukuku, Y. Kervella, V. K. Challuri, F. Sauvage, S. Narbey, P. Maldivi, C. Aumaître and R. Demadrille, *Chem. Sci.*, 2023, **14**, 8497–8506.

30 H. Fang, J. Ma, M. J. Wilhelm, B. G. DeLacy and H.-L. Dai, *Part. Part. Syst. Charact.*, 2021, **38**, 2000220.

31 W. Xiang, F. Huang, Y.-B. Cheng, U. Bach and L. Spiccia, *Energy Environ. Sci.*, 2012, **6**, 121–127.

32 F. Bella, S. Galliano, C. Gerbaldi and G. Viscardi, *Energies*, 2016, **9**, 384.

33 J. Fan, Y. Hao, A. Cabot, E. M. J. Johansson, G. Boschloo and A. Hagfeldt, *ACS Appl. Mater. Interfaces*, 2013, **5**, 1902–1906.

34 K. Kannankutty, C.-C. Chen, V. S. Nguyen, Y.-C. Lin, H.-H. Chou, C.-Y. Yeh and T.-C. Wei, *ACS Appl. Mater. Interfaces*, 2020, **12**, 5812–5819.

35 M. Freitag, J. Teuscher, Y. Saygili, X. Zhang, F. Giordano, P. Liska, J. Hua, S. M. Zakeeruddin, J.-E. Moser, M. Grätzel and A. Hagfeldt, *Nat. Photonics*, 2017, **11**, 372–378.

36 M. Freitag, Q. Daniel, M. Pazoki, K. Sveinbjörnsson, J. Zhang, L. Sun, A. Hagfeldt and G. Boschloo, *Energy Environ. Sci.*, 2015, **8**, 2634–2637.

37 W. Yang, M. Söderberg, A. I. K. Eriksson and G. Boschloo, *RSC Adv.*, 2015, **5**, 26706–26709.

38 S. Pelet, J.-E. Moser and M. Grätzel, *J. Phys. Chem. B*, 2000, **104**, 1791–1795.

39 S. Nakade, T. Kanzaki, W. Kubo, T. Kitamura, Y. Wada and S. Yanagida, *J. Phys. Chem. B*, 2005, **109**, 3480–3487.

40 G. Boschloo, L. Häggman and A. Hagfeldt, *J. Phys. Chem. B*, 2006, **110**, 13144–13150.

41 Y. Wang, J. Lu, J. Yin, G. Lü, Y. Cui, S. Wang, S. Deng, D. Shan, H. Tao and Y. Sun, *Electrochim. Acta*, 2015, **185**, 69–75.

42 J.-Y. Kim, J. Y. Kim, D.-K. Lee, B. Kim, H. Kim and M. J. Ko, *J. Phys. Chem. C*, 2012, **116**, 22759–22766.

43 J. Halme, P. Vahermaa, K. Miettunen and P. Lund, *Adv. Mater.*, 2010, **22**, E210–E234.

44 L. P. Teo, T. S. Tiong, M. H. Buraidah and A. K. Arof, *Opt. Mater.*, 2018, **85**, 531–537.

45 J. Zhang, Y. Cui, X. Zhang, Q. Sun, J. Zheng, P. Wang, J. Feng and Y. Zhu, *C. R. Chim*, 2013, **16**, 195–200.

46 G. M. Tina, C. Ventura, S. Ferlito and S. De Vito, *Appl. Sci.*, 2021, **11**, 7550.

47 J. F. Gaviria, G. Narváez, C. Guillen, L. F. Giraldo and M. Bressan, *Renewable Energy*, 2022, **196**, 298–318.

48 C. She, Q. Huang, C. Chen, Y. Jiang, Z. Fan and J. Gao, *J. Mater. Chem. A*, 2021, **9**, 25168–25177.

49 J. Li, B. Pradhan, S. Gaur and J. Thomas, *Adv. Energy Mater.*, 2019, **9**, 1901891.

50 Y. Liu, X. Tan, J. Liang, H. Han, P. Xiang and W. Yan, *Adv. Funct. Mater.*, 2023, **33**, 2214271.

51 X. Du, L. Lüer, T. Heumueller, J. Wagner, C. Berger, T. Osterrieder, J. Wortmann, S. Langner, U. Vongsaysy, M. Bertrand, N. Li, T. Stubhan, J. Hauch and C. J. Brabec, *Joule*, 2021, **5**, 495–506.

52 Q. Zhang, Y. J. Zheng, W. Sun, Z. Ou, O. Odunmbaku, M. Li, S. Chen, Y. Zhou, J. Li, B. Qin and K. Sun, *Adv. Sci.*, 2022, **9**, 2104742.

53 N. Meftahi, M. Klymenko, A. J. Christofferson, U. Bach, D. A. Winkler and S. P. Russo, *npj Comput. Mater.*, 2020, **6**, 1–8.

54 W. Sun, Y. Zheng, K. Yang, Q. Zhang, A. A. Shah, Z. Wu, Y. Sun, L. Feng, D. Chen, Z. Xiao, S. Lu, Y. Li and K. Sun, *Sci. Adv.*, 2019, **5**, eaay4275.

55 Q. Arooj and F. Wang, *Sol. Energy*, 2019, **188**, 1189–1200.

56 Y. Wen, L. Fu, G. Li, J. Ma and H. Ma, *Sol. RRL*, 2020, **4**, 2000110.

57 S. S. Sutar, S. M. Patil, S. J. Kadam, R. K. Kamat, D. Kim and T. D. Dongale, *ACS Omega*, 2021, **6**, 29982–29992.

58 G. R. Kandregula, D. K. Murugaiah, N. A. Murugan and K. Ramanujam, *New J. Chem.*, 2022, **46**, 4395–4405.

59 D. Padula, J. D. Simpson and A. Troisi, *Mater. Horiz.*, 2019, **6**, 343–349.

60 Y. Wu, J. Guo, R. Sun and J. Min, *npj Comput. Mater.*, 2020, **6**, 1–8.

61 B. Cao, L. A. Adutwum, A. O. Oliynyk, E. J. Luber, B. C. Olsen, A. Mar and J. M. Buriak, *ACS Nano*, 2018, **12**, 7434–7444.

62 A. Kirkey, E. J. Luber, B. Cao, B. C. Olsen and J. M. Buriak, *ACS Appl. Mater. Interfaces*, 2020, **12**, 54596–54607.

63 D. He, Y. Hu, J. Tao, X. Zheng, H. Liu, G. Jing, H. Lu, H. Guan, J. Yu, J. Zhang, J. Tang, Y. Luo and Z. Chen, *Opt. Mater. Express, OME*, 2017, **7**, 264–272.

64 S. E. Koops, B. C. O'Regan, P. R. F. Barnes and J. R. Durrant, *J. Am. Chem. Soc.*, 2009, **131**, 4808–4818.

65 C. Aumaitre, C. Rodriguez-Seco, J. Jover, O. Bardagot, F. Caffy, Y. Kervella, N. López, E. Palomares and R. Demadrille, *J. Mater. Chem. A*, 2018, **6**, 10074–10084.

66 C. J. Traverse, R. Pandey, M. C. Barr and R. R. Lunt, *Nat. Energy*, 2017, **2**, 849–860.

67 J. M. Park, C. Y. Jung, W.-D. Jang and J. Y. Jaung, *Dyes Pigm.*, 2020, **177**, 108315.

68 J. Idígoras, G. Burdziński, J. Karolczak, J. Kubicki, G. Oskam, J. A. Anta and M. Ziółek, *J. Phys. Chem. C*, 2015, **119**, 3931–3944.

69 J. Wu, Z. Lan, J. Lin, M. Huang, Y. Huang, L. Fan and G. Luo, *Chem. Rev.*, 2015, **115**, 2136–2173.

70 K. Zhang, C. Qin, X. Yang, A. Islam, S. Zhang, H. Chen and L. Han, *Adv. Energy Mater.*, 2014, **4**, 1301966.

71 A. V. Chernyshev, E. V. Solov'eva, I. A. Rostovtseva, N. A. Voloshin, O. P. Demidov, K. E. Shepelenko and A. V. Metelitsa, *Mendeleev Commun.*, 2022, **32**, 531–533.

72 A. Abdollahi, H. Roghani-Mamaqani and B. Razavi, *Prog. Polym. Sci.*, 2019, **98**, 101149.

73 A. Yella, S. Mathew, S. Aghazada, P. Comte, M. Grätzel and M. K. Nazeeruddin, *J. Mater. Chem. C*, 2017, **5**, 2833–2843.

74 W. Yang, N. Vlachopoulos, Y. Hao, A. Hagfeldt and G. Boschloo, *Phys. Chem. Chem. Phys.*, 2015, **17**, 15868–15875.

75 J. Cong, Y. Hao, G. Boschloo and L. Kloo, *ChemSusChem*, 2015, **8**, 264–268.

76 Z. Zhang, P. Chen, T. N. Murakami, S. M. Zakeeruddin and M. Grätzel, *Adv. Funct. Mater.*, 2008, **18**, 341–346.

77 E. Zimmermann, P. Ehrenreich, T. Pfadler, J. A. Dorman, J. Weickert and L. Schmidt-Mende, *Nat. Photonics*, 2014, **8**, 669–672.

78 J. P. Gonzalez-Vazquez, G. Oskam and J. A. Anta, *J. Phys. Chem. C*, 2012, **116**, 22687–22697.